applied sciences

MDPI

Article

Additive Manufacturing for Lightweighting Satellite Platform

Alberto Boschetto, Luana Bottini *, Luciano Macera and Somayeh Vatanparast

Mechanical and Aerospace Engineering Department, Sapienza University of Rome, Via Eudossiana 18, 00184 Rome, Italy

* Correspondence: luana.bottini@uniroma1.it

Featured Application: The research provided in this work assists engineers in developing new designs for lightweight, stronger, and more efficient satellite platform structures that can be built via additive manufacturing. The examination of the aspects that may impact the dimensional correctness and repeatability of the structure gives practical knowledge about 3D printing production, which requires the usage of various designs. The findings identified design strategies for lattice structures, including local optimization, which allow satisfying stringent satellite requirements.

Abstract: Lightweight structures with an internal lattice infill and a closed shell have received a lot of attention in the last 20 years for satellites, due to their improved stiffness, buckling strength, multifunctional design, and energy absorption. The geometrical freedom typical of Additive Manufacturing allows lighter, stiffer, and more effective structures to be designed for aerospace applications. The Laser Powder Bed Fusion technology, in particular, enables the fabrication of metal parts with complex geometries, altering the way the mechanical components are designed and manufactured. This study proposed a method to re-design the original satellite structures consisting of walls and ribs with an enclosed lattice design. The proposed new structures must comply with restricted requirements in terms of mechanical properties, dimensional accuracy, and weight. The most challenging is the first frequency request which the original satellite design, based on traditional fabrication, does not satisfy. To overcome this problem a particular framework was developed for locally thickening the critical zones of the lattice. The use of the new design permitted complying with the dynamic behavior and to obtain a weight saving maintaining the mechanical properties. The Additive Manufacturing fabrication of this primary structure demonstrated the feasibility of this new technology to satisfy challenging requests in the aerospace field.

Keywords: laser powder bed fusion; design for additive manufacturing; satellite platform; lattice structure; aerospace application

Citation: Boschetto, A.; Bottini, L.; Macera, L.; Vatanparast, S. Additive Manufacturing for Lightweighting Satellite Platform. *Appl. Sci.* **2023**, *13*, 2809. https://doi.org/10.3390/app13052809

Academic Editor: Paulo Santos

Received: 11 January 2023
Revised: 14 February 2023
Accepted: 20 February 2023
Published: 22 February 2023

1. Introduction

For decades, minisatellites have demonstrated their capability in complex missions and have made essential contributions to space science in multiple disciplines. Small satellites have attracted industrial attention due to their flexibility, rapid development, resilience, low cost, and risk tolerance in cutting-edge technology. Furthermore, because they have the ability to replace huge systems, they have altered the space industry in the satellite sector during the previous several years [1].

In the Small-Sat class, minisatellites have more available power, larger payload mass, and more capable radio systems that can transmit more data than the smaller satellite categories [2,3]. It is common for minisatellites to include propulsive capabilities for orbit adjustments and orientation, encrypted communications, and fine pointing that are beyond the reach of smaller containerized platforms. Minisatellites are becoming increasingly important in low Earth orbit and Geostationary Equatorial Orbit (GEO) and are likely to have a more significant presence in deep space in the coming years [4].

In 2013, 247 CubeSats and 105 additional non-CubeSat small spacecraft weighing less than 50 kg were launched into orbit, accounting for less than 2% of the total mass sent into orbit across several years. In 2013, almost 60% of all spacecraft launched weighed less than 600 kg, with 83% weighing less than 200 kg and 37% being nanosatellites; 94% of the 1282 spacecraft launched in 2020 were tiny spacecraft having an overall mass of less than 600 kg, with 28% being under 200 kg and 9% being nanosatellites. Since 2013, the demand for small spacecraft has climbed by more than 30%, becoming the key source of space access for commercial, government, private, and academic entities [5].

A satellite is composed of several parts, which vary depending on the type of application and orbit. Two elements, however, are common to all satellites and are called payload and platform [6]. The platform is the part of the satellite that carries the payload and all its equipment in space. It is the vital part, as it keeps the rest of the satellite together and allocates power, propulsion, and data processing systems. The platform also contains devices that allow communication with terrestrial control stations. The primary structure, usually made of aluminum or carbon fibers, must be strong enough to survive unharmed by the inertial loads: the carrying of satellite mass, and during the launch the accelerations are up to 8 g [7]. In addition, it shall be stiff enough to separate the satellite's global dynamic behavior from launch system one and avoid the risk of destructive couplings among them. In fact, this coupling could impair the onboard item alignments/pointing and, in the worst cases, damage the structural integrity too [8].

Over the past decade, several commercial families of small satellites have been developed by providing the technological framework for launching systems with specific functions into orbit without worrying about technologies related to the launch, propulsion, flight, power supply and data links [9].

The Evolved Expendable Launch Vehicle (EELV) Secondary Payload Adapter (ESPA), which is a specific adapter for launching secondary payloads on orbital launch vehicles, was developed for small satellites [9]. Although it was originally developed for US military launches in the 2000s, the adapter design has become a de facto standard and is now also used for spaceflight missions on commercial missions as well. For example, multiple ESPA rings were used on SpaceX Falcon 9 [10].

Small satellites encompass a wide variety of miniature spacecraft, typically identified by their mass. NASA small spacecraft definitions (Small-Sat) [9] set the upper mass limit to 180 kg, which corresponded to the original ESPA secondary payload mass limit, and defined the following categories: Minisatellite 100–180 kg, Microsatellite 10–100 kg, Nanosatellite 1–10 kg, Picosatellite <1 kg, and CubeSat. Less frequently, the range for minisatellites is extended to 1000 kg [11].

A new carrying structure, called VESPA (Vega Secondary Payload Adapter) dedicated to Vega launchers was developed by European Supervisory Authorities (ESA). VESPA can carry a 1000 kg main satellite on the top and a secondary payload of 600 kg in the internal cone. The Small Spacecraft Mission Service (SSMS) modular dispenser can accommodate any combination of 1 kg CubeSats up to 500 kg minisatellites, from a main large satellite with smaller companions to multiple small satellites, or dozens of individual CubeSats [12]. In Figure 1 an SSMS representation is shown with different types of small satellites hosted in two main sections, the hexagonal lower section takes a dozen CubeSats or six small satellites while the upper section is used for micro, minisatellites and small satellites. Both sections can also be used independently.

Manufacturing in the aerospace industry is subject to various interactive technical and economic goals, including functional performance, cycle time reduction, weight reduction, complexity, cost control, and sustainability. Each of these objectives is intertwined, and each component must be carefully addressed when selecting an ideal design solution. The relative relevance of these aims is determined by the unique aeronautical application [13]. Structure technical performance and permitted mission-defined payload are constrained, which means that reducing system mass directly correlates to improved economic and

technical performance, such as lower fuel costs, lower emissions, greater payloads, and extended range [14].

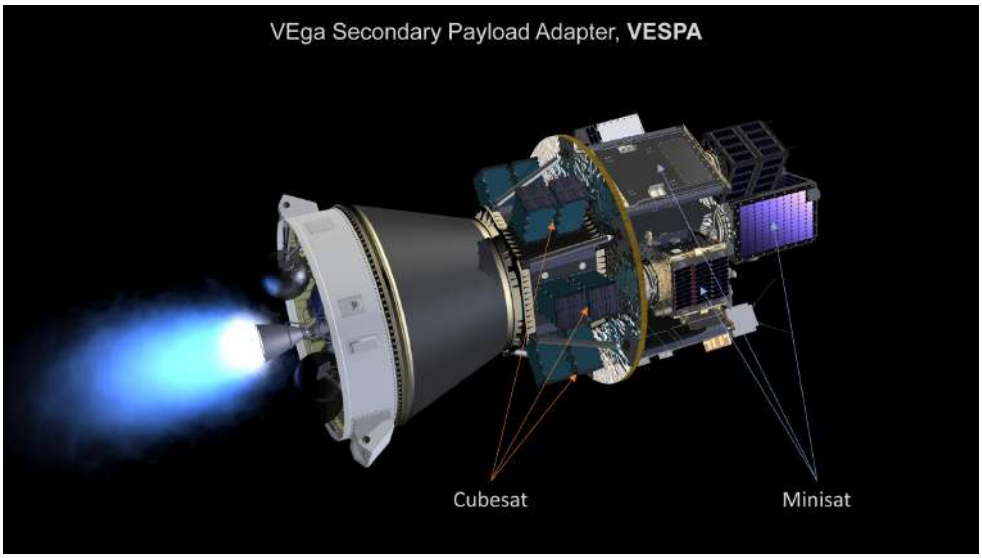

Figure 1. SSMS representation with different types of small satellites (copyright of ESA-J. Huart).

One of the primary reasons for using Additive manufacturing (AM) in aircraft is the huge cost savings and shorter lead time that can be achieved when compared to traditional production [15]. It is generally cheaper and faster for low-number, geometrically complex parts that would require time-consuming and complex machining [16]. Aerospace components are complicated and frequently need unique alloys with extensive procurement lead time in a wrought form, as well as substantial processing time to shape, machine, fabricate, or assemble. The different inspections and traceability requirements of materials and parts are carried out throughout the process, notably increasing the lead time. AM provides a significant opportunity to cut costs via an efficient supply chain and reduced lead time, as well as logistical benefits [17]. There are various examples of cost savings and lead time reductions [18].

AM is being recognized as a fabrication technology that delivers revenue to the aerospace industry throughout its supply chain and repair operations [15]. In 2017, Boeing began using at least four AM titanium alloy parts to produce its 787 Dreamliner aircraft, with near-term plans to manufacture nearly 1000 parts through AM to save $23 million per aircraft [19]. Airbus, another major player in AM space, has installed AM metal brackets and vent tubes on Airbus A320neo and the A350 XWB test aircraft [20]. NASA, the European Space Agency, SpaceX, Honeywell Aerospace, Lockheed Martin, and Northrop Grumman are exploring the use of AM igniters, injectors and combustors in their rocket engines.

Given the low production rate of satellites and launch vehicles in the space industry, AM technology could pave the way for lighter and more sophisticated parts.

Another important AM benefit is part consolidation. Traditionally, complicated aerospace components are made up of several basic elements that are connected with various types of fasteners (welds, bolts, and brazes). When compared to a single part, such assemblies have inferior reliability and higher inspection, tooling, and maintenance costs [21]. For example, the Eurostar E3000 satellite used an Airbus 3-D-printed aluminum element. The 3D printed brackets not only weighed up to 35% less than the original traditional form and were 40% stiffer, but they were also built as a single part to replace an assembly consisting of numerous metal components and up to 44 rivets saving material waste and making assembly easier [22]. The CubeSat bus construction requires about 150 pieces to be machined in typical production. The United States Air Force Institute of Technology (AFIT) employed nTopology to lower the weight and production time of a CubeSat bus using AM: the obtained bus fabricated in Inconel 718 was 50% lighter and

20% stiffer than the original aluminum assembled [23]. Furthermore, geometrical inaccuracies and undesirable misalignments or deflections of these components may exceed acceptable tolerances [24]. The AM redesign can reduce a multi-part assembly made up of numerous components into a single part with the same operational functionality [25–27]. With reference to Laser Powder Bed Fusion (PBF-LB/M), it is possible to mention some successful cases of high-rate production in the aerospace market. In [28] an engine heat exchanger, traditionally composed of 163 parts, was consolidated into one single object. This way the costs associated with the assembly and the welding, as well as an entire class of failure mechanisms and their nondestructive evaluation, were eliminated. In [29] 28 fuel nozzles were printed via PBF-LB/M finding an optimal configuration that reduced the cost savings and helped to solve problems of fuel mixing and fuel emissions. When compared to traditional manufacturing processes, the GE9X heat exchanger offers a 40% mass reduction and a 25% cost reduction while integrating 163 components into a single part.

Of the most notable advantages of PBF-LB/M is the capability to manufacture parts with complex geometry such as lattice structures. They are cellular structures with periodical configurations of unit cells in two or three dimensions. The lattice structure might give good characteristics, including a superior strength/weight ratio, good thermal properties, and acoustic shielding, making it perfect for high-profit industrial objectives such as aerospace [30]. The more important feature of lattice structures is the best structural efficiency per unit weight [31]. In [32] the pumping system holder for the Dust Complex payload for the ExoMars 2022 mission's Surface Science Platform was designed and fabricated in PBF-LB/M. Sensitivity and optimization tests on AMed components based on simple honeycomb cells were carried out in order to discover the most promising arrangement for a space instrument's pumping system holder. In terms of dynamic behavior and strength vs design loads, several shapes were examined. The optimum option was a honeycomb thin-walled structure (0.3 mm thickness), whose topology and elementary cell size was adjusted to decrease bulk while meeting all design criteria. According to the tests, cast alloy displays lower ultimate tensile stress (240–270 MPa) than the $AlSi_9Cu_3$ alloy manufactured by AM (374–440 MPa). The evaluation revealed that hexagonal honeycomb lattice configurations provide the greatest specific stiffness and strength.

In [33] a honeycomb satellite panel was substituted by a lattice sandwich revealing improved benefits in terms of stiffness, strength, connections, special-shaped structural configuration, lightweight, and fabrication cycle. The lightweight satellite construction which is built entirely of lattice sandwich panels using PBF-LB/M shows a weight-to-satellite weight ratio of 7.7%, which is far superior to the 15–25% ratio of minisatellites (satellites weighing 100 to 500 kg) composed of standard aluminum honeycomb sandwich panels. When this satellite structure is subjected to a high frequency loading with an amplitude equivalent to the real-world service situation, the unaltered eigenfrequencies demonstrate that no structural damage occurs during testing. As a result, the resonance frequency of the satellite structure composed of lattice sandwich panels can be much greater than that of the same-weight aluminum honeycomb panels.

An ultralightweight bracket structure for a satellite was attained in [34] utilizing a topology optimization-based lattice infill technique.

In [35], an octagonal truss lattice structure is used to construct a lightweight compressor impeller. The mass of the impeller is reduced from 195.3 g to 149.4 g after the solid portion inside the hub was replaced with a lattice construction. The residual deformation of the lattice compressor impeller may be decreased by 20.19% when compared to the solid compressor impeller. The residual stress of the lattice compressor impeller may be lowered by 8.72%.

In [36] a lightweight phase-change thermal controller structure based on lattice cells is presented. The structure is made completely of AlSi10Mg using PBF-LB/M. The structure's mass was 190 g, which is 60% lighter than most typical constructions of the same size (500–600 g). The thermal controller absorbs 60 J/cm^2 of heat energy per unit area. The energy capabilities of thermal controllers of the same size built using a conventional process,

on the other hand, are around 40 J/cm^2. Therefore, the thermal capacity of the lattice-based thermal controller was improved by 50% when compared to typical controllers of the same volume.

Besides these relevant properties, materials fabricated by PBF-LB/M shows differences between the corresponding alloys fabricated via traditional methods such as casting and forging. The rapid cooling results in a non-equilibrium solidification process leading to grain refinement, the formation of metastable phases, and preferential grain growth [37]. The aluminum alloys exhibit a very fine microstructure as compared to the traditional methods such as casting, forging, extrusion and powder metallurgy which can provoke defects in the final produced parts [38]. The low cooling rate of a traditional casting process determines a coarse microstructure, and many other defects such as shrinkage porosity, slag inclusion and element segregation decrease the mechanical properties of the fabricated part [39]. Conversely, the strength of a part produced by PBF-LB/M is increased by the in-situ formation of an amorphous, ultrafine-grained structure, especially in Si-rich aluminum such as AlSi10Mg [40,41]. This fine microstructure permits improving hardness, tensile and compressive strengths, fatigue performance, creep, impact, and wear resistance; the only drawback that remains is the lack of ductility which can be solved by using thermal treatments. [42]. Nevertheless, some specific defects such as thermally induced residual stresses, gas porosities, oxide layers, and un-melted material can occur during the PBF-LB/M process [43]. As a result, the crack initiation and propagation can be facilitated resulting in significantly reduced fatigue properties with respect to the same material manufactured by casting or forging [44]. Another issue limiting the PBF-LB/M is the attainable roughness, which is affected by the balling phenomenon, pores, and satellite that can be reduced by optimal selection of the processing parameters but not eliminated; also, the accuracy of as-built parts, are poorer than the wrought and machined counterparts [45]. The PBF-LB/M surface finish significantly impacts high-frequency applications resulting in microwave loss and requiring post-processing techniques [46]. Lastly, tribological performance is lower than traditional AlSi10Mg cast alloy [47].

Despite these drawbacks, PBF-LB/M shows outstanding advantages in manufacturing complex-shaped parts such as a lattice structure giving a part design with an exceptional degree of freedom. The present work investigates ways to redesign and fabricate PBF-LB/M modular platforms of satellites made by lattice structures. The major aim was to satisfy the critical request of the first natural frequency which is not accomplished by the original design of the satellite manufactured by traditional technologies. This goal is challenging if coupled with the module lightweighting. The paper illustrates how to employ the AM for the real industrial production of this big component. For this purpose, the highest layer thickness of 90 µm was employed to increase productivity and provide competitive fabrication. Cares and strategies were selected to deal with the reduced material strength and provide reliable fabrication. Thus, an easy-to-print lattice was identified, and the large and thin walls were CNC machined afterward. The optimized design was carried out including the junction points and the thermal plates. Experimental verification allowed us to demonstrate the capability of the proposed work.

2. Materials and Methods

2.1. Component

To introduce the PBF-LB/M technology in the primary structure elements, a dedicated design phase has been carried out moving from the traditional structural schemes towards a more efficient and additively manufactured solution. Specifications range covers the weight, the modal behavior and the protection of the electronics from the space environment [48].

The main requirements for the satellite platform are:

- Reduced mass.
- Modal behavior: $\geq$38 Hz.
- Radiation shielding: wall thickness $\geq$ 1 mm.

The third requirement takes effect on the mass range. The minimum mass of a component characterized by the minimum wall thickness is about 37% of the original design. Additionally, since the minimum first natural frequency is not satisfied, a reasonable target for the optimized weight is 80%.

2.2. Selected AM Technology and Material

The chosen AM technology in this study is the PBF-LB/M, one of the most often used techniques of the powder-bed fusion category for metals processing [49,50]. It uses the thermal energy provided by a laser source to selectively melt and consolidate regions of a powder bed. This way it is possible to fabricate layer by layer full dense metallic components characterized by very complex geometries [26,51].

When considering small spacecraft constructions, material selection is critical. Physical qualities (density, thermal expansion, and radiation resistance) as well as mechanical properties (modulus, strength, and toughness) must be met. Aluminum alloys have been used in the aircraft industry since its commencement. Because of its low cost, light weight, high strength-to-weight ratio, and simplicity of manufacture, aluminum was the most widely used material in aircraft until recent developments in composite technologies [13]. For the specific case of this work, the choice of material was constrained by several factors, both technological and design. The need for lightness steered the choice toward light alloys; the specification that the structure also has a heat exchange function ruled out titanium alloys, focusing the choice on aluminum ones. Needing to have the highest possible Technology Readiness Level, the choice was oriented toward the AlSi10Mg, processable with all industrial-grade metal PBF-LB/M machines. The chemical composition of the employed powder supplied by EOS is reported in Table 1.

Table 1. Chemical composition of the employed powder.

Si	Fe	Cu	Mn	Mg	Ni	Zn	Pb	Sn	Ti	Al
9–11	≤0.55	≤0.05	≤0.45	0.20–0.45	≤0.05	≤0.10	≤0.05	≤0.05	≤0.15	Bal.

The particle size distribution is measured by the D50, D10 and D90 paraments which are 29.2 µm, 16.4 µm and 40.3 µm, respectively.

2.3. Fabrication

For the fabrication, two EOS machines based on Direct Metal Laser Sintering (DMLS) technology were selected: an EOS M290 (EOS GmbH-EOS Additive Manufacturing, Krailling, Germany) was used for preliminary testing and an EOS M400 (EOS GmbH-EOS Additive Manufacturing, Germany) was employed for prototype fabrication. EOS M290 is equipped with a 400 W ytterbium fiber continuum laser characterized by a beam spot diameter of 100 µm and a building volume of 250 × 250 × 325 mm^3; using a typical layer thickness of 30 µm, the max volume rate is 5.1 mm^3/s. The process was carried out in an argon inert atmosphere with less than 0.1% oxygen and the building platform was preheated at 200 °C to reduce residual stresses.

EOS M400 is equipped with a 1000 W ytterbium fiber continuum laser characterized by a beam spot diameter of 90 µm and a building volume of 400 × 400 × 400 mm^3; with the layer thickness set to 90 µm, the max volume rate is 27.8 mm^3/s. The process was carried out in an argon inert atmosphere with less than 0.2% oxygen and the building platform was preheated at 165 °C to reduce residual stresses. The processing parameters have a direct effect on the final component behavior creating unique micro- and macro-structures due to the repeated extremely fast melting and cooling of the material. Optimized combinations of the laser power, the hatch distance, the layer thickness, the scanning speed and scanning strategies can lead to desired outcomes concerning the final microstructures, the corrosion resistance, the residual porosity, the mechanical properties, and the stress-

induced distortions [43]. Many authors evaluated the combined effect of the exposure parameters by using a factor called Volumetric Energy Density (VED) defined as:

$$VED = P/(V_s \cdot h_d \cdot L_T) \quad (1)$$

where P is the laser power, V_s is the scanning speed, h_d is the hatch distance, and L_T is the layer thickness. At low layer thickness, a VED of about 50 J/mm^3 leads to high density, good surface roughness and mechanical performance [52,53]. At high layer thickness, typically chosen for high productivity, the employment of a high laser power corresponds to the selection of lower hatch distance resulting in a comparable VED [54]. In Table 2 the main characteristics of the two employed machines are summarized together with the exposure parameters.

Table 2. Summary of machines characteristics and exposure parameters used for fabrication.

	EOS M290	**EOS M400**
Laser type	Ytterbium fiber continuum	Ytterbium fiber continuum
Laser number	1	1
Laser max power	400 W	1000 W
Working volume	250 × 250 × 325 mm^3	400 × 400 × 400 mm^3
Volume rate	5.1 mm^3/s (with 30 µm layer)	27.8 mm^3/s (with 90 µm layer)
	Exposure parameters	
Laser Power	370 W	600 W
Hatch distance	0.19 mm	0.1 mm
Scanning speed	1300 mm/s	1450 mm/s
Layer thickness	30 µm	90 µm
Volumetric Energy Density	49.93 J/mm^3	45.98 J/mm^3

Since large walls with a small thickness of 0.5 mm are difficult to achieve with PBF-LB/M systems and surface roughness could compromise mechanical performance, additional material was provided. The required roughness and thickness were assured by CNC machining. Hence, the machining allowances are:

- +0.5 mm additional material on skins
- +1.0 mm additional material on all junction point planes
- +1.0 mm additional material on upper junction point teeth
- holes for module connection and screw inserts are closed.

PBF-LB/M manufacturing preprocessing was performed using Materialise Magics 23.01 (Materialise, Leuven, Belgium). The part orientation was dictated by the wide thin walls and was vertically positioned. The support structures were generated and, together with the model, were uploaded in EOSPRINT 2.4 (EOS GmbH-EOS Additive Manufacturing, Krailling, Germany) software in the required formats. Here, the exposure parameters were assigned, and the laser path was simulated and checked before the build phase.

Specific calibration operations were performed to ensure the best performance in producing the design geometries.

After fabrication, parts undergo a preliminary dimension check before proceeding with the heat treatment. The heat-induced laser melting process causes considerable residual stress and, as a result, dimensionally unstable parts [55]. A stress relieving heat treatment in a Nabertherm LH120/14 (Nabertherm GmbH, Lilienthal, Germany) controlled atmosphere hoven was applied according to the following characteristics. The building platform with the parts still attached was subjected to heat treatment to minimize possible distortion due to the variation of internal stresses in the material. The parts were slowly heated at a 5 °C/min rate up to the soaking temperature of 300 °C and maintained for 2 h; after, cooling at a 5 °C/min rate was performed.

Detachment from the building platform was carried out through wire Electrical Discharge Machining (EDM) technology using the U6 H.E.A.T. Extreme Wire (Makino, Japan) machine to reduce mechanical stress and to have a clean, flat surface in the underside of the parts. After parts detachment, a second preliminary dimension check was performed. Once part machinability is confirmed by adimension check, each part is CNC machined individually. The employed machine is a five-axis machining center S616 (C.B. Ferrari, Italy). Custom gripping equipment was designed and used to hold the part for the removal of 0.5 mm onto the wall skins. An assembly jig was developed for finishing the junction points and the screw inserts to guarantee overall dimensions and perform assembly operations. It is made of tempered steel, machined into two plates each one with a 5 mm-deep groove with a tolerance of 0.04 mm from edge to edge to facilitate assembly while ensuring tolerance compliance (Figure 2a). The plates are aligned and connected by vertical rods and also have rectangular openings for each junction point to allow for final CNC milling operations and a set of inserts and positioning pins (Figure 2b). The configuration during the real assembly operations is shown in Figure 2.

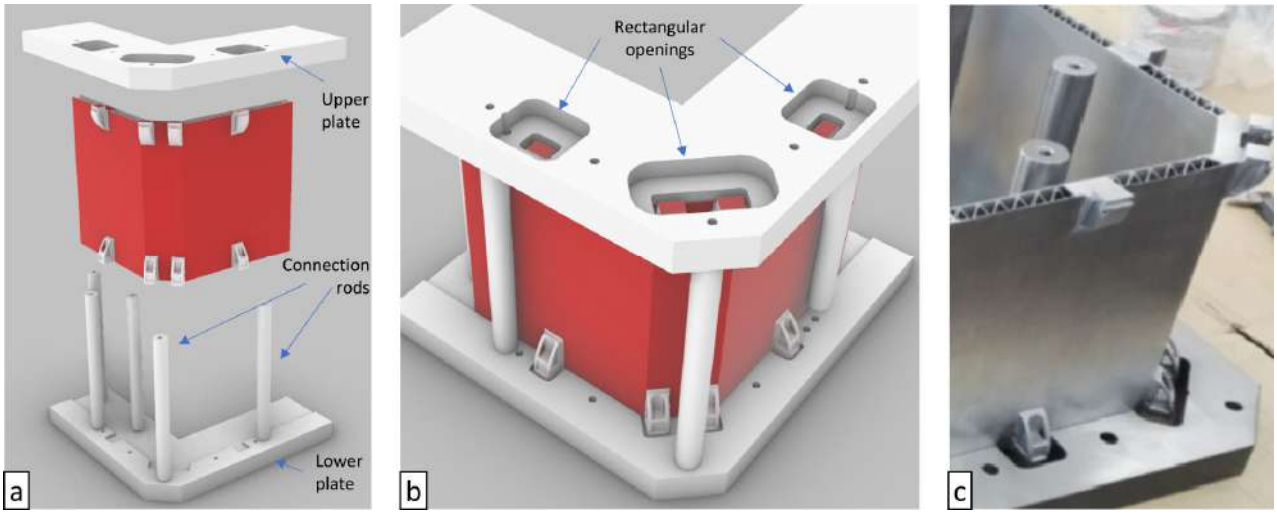

Figure 2. Exploded diagram of the assembly jig (**a**), assembled jig schematic (**b**) and real part during assembly (**c**). Surfaces to be machined are indicated in red.

As part of quality assurance, a tensile test was carried out to validate the AM process on the specimen printed in the same building platform of the parts. A 50 kN Zwick Z050TN (ZwickRoell GmbH & Co. KG, Ulm, Germany) universal testing machine was employed under quasi-static loading conditions, imposing a ramped displacement at 0.05 mm/min speed. The sample geometry was a dog bone, with a square cross-section of 5.72×4.00 mm^2 and a nominal gauge length of 25.40 mm in accordance with the standard ASTM E8/E8M [56].

3. Structure Design and Optimization

3.1. Lattice Design

All original designs of the two types of modules consisted of an outer skin with reinforcing ribs and a coupling interface, characterized by the specifications reported in Table 3. In Figure 3 the modules are shown together with the structural load cases.

The modal behavior specification is particularly critical to the extent that the original design cannot satisfy it. In fact, the first natural frequency was 23 Hz. The approach for the part re-design was to fully exploit AM advantages starting from the basic idea of a wall composed of two thin skins connected by a lattice structure, thus abandoning the traditional "wall with ribs" based solutions. The two different designs including the traditional one and the lattice solution are presented in Figure 4.

Table 3. Original design specification and structural loads.

	MODULE 1	MODULE 2
Material	Aluminum	Aluminum
Mass	2.78 kg	5.26 kg
Dimensions—h	200 mm	150 mm
Dimensions—plant	600 mm × 600 mm	600 mm × 600 mm
Dimensions—wall thickness	1 mm	1 mm
Dimensions—wall thickness (overall)	5 mm	5 mm
Features	Ribs	Ribs
Modal behavior	≥38 Hz	≥38 Hz
Structural Loads (Case 1)	10.5 kN compression, 6.2 kN lateral	
Structural Loads (Case 2)	6.2 kN traction, 4.4 kN lateral	

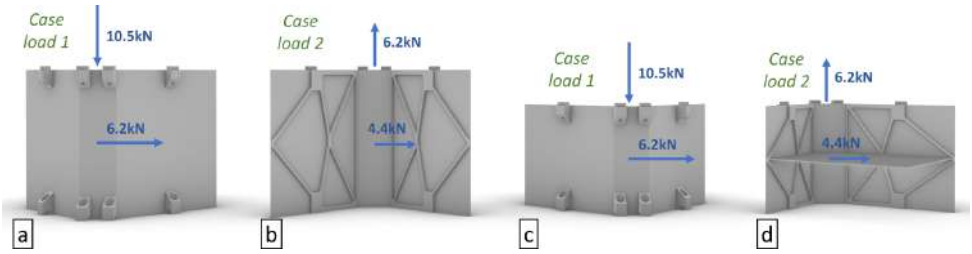

Figure 3. Sketch of module 1 (**a**,**b**) and module 2 (**c**,**d**) with the indication of the structural load for case 1 (**a**,**c**) and case 2 (**b**,**d**).

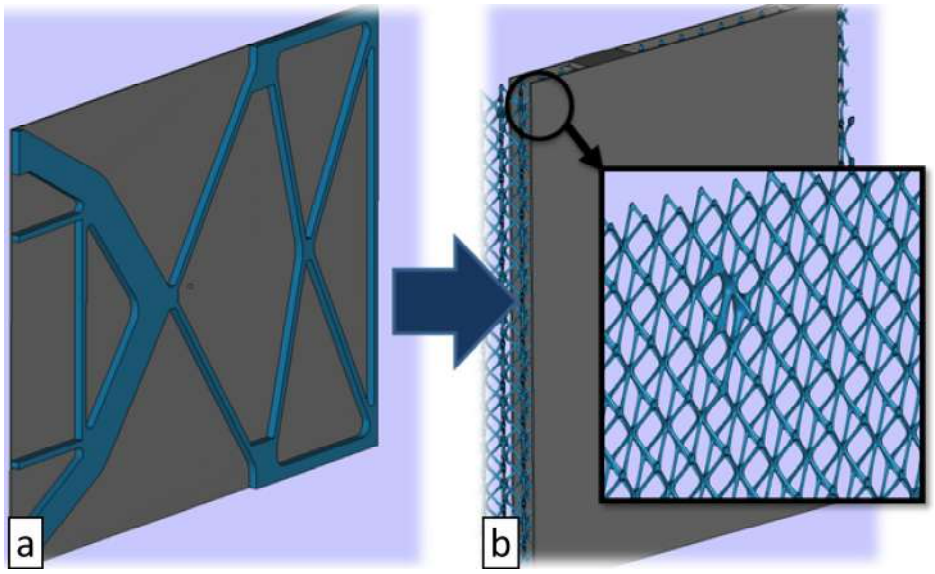

Figure 4. From traditional wall with ribs technology (**a**) to AM technology solution (**b**).

Lattice structures are an attractive option for lightweighting applications and many cell topologies were investigated. An interesting type is the triply periodic minimal surfaces (TPMS) [57], namely a kind of periodic surface with zero mean curvature described by an implicit mathematical formulation that can be altered to tune its mechanical performance [58]. They were originally discovered by Schwarz in 1865 who invented the well-known Gyroid (Figure 5a), Primitive (Figure 5b) and Diamond (Figure 5c). Lately, his student Nevious discovered the TPMS shown in Figure 5d. The Schoen I-WP exhibits viscoelastic behavior (Figure 5e). The Fischer–Koch S Surface (Figure 5f) has no mirror symmetry which leads to an anisotropic elastic behavior. The potential of AM can be empowered by considering these minimal surfaces; however, some possible issues must be considered. The PBF-LB/M technology has critical problems in the down skin, particularly

with selected aluminum alloys and these TPMS present overhanging zones and even horizontal walls. To have an acceptable roughness it is preferable that the surface angles do not fall below 45°. Moreover, the Gyroid, the Diamond, and the Fischer–Koch S show intricate cavities: in this application, they must be included in relatively thin components, hence the cavities must be very small. This issue is increased by the use of a 1 mm wall thickness. As the component is very large, the powder removal at the end of the fabrication is challenging for TPMS and they were excluded from the satellite design. A tailored "star-shaped" lattice that ensured printability without supports, as well as symmetric mechanical characteristics was introduced. Lattice type and basic dimensions were determined by taking into account both AM compatibility and structure requirements (void to full ratio equal to 5%). In particular, the chosen basic element is reasonably easy to print and offers good thermal and mechanical properties making it ideal for applications in the aerospace environment where thermal management capability is crucial [59]. The cell size was chosen according to the total wall thickness. For instance, the first type was 5×5 mm^2 size in a plant. In order to allow a self-supporting surface of arms, the height of the cell was set to 8 mm: this way the lowest overhanging angle was 48.53° which is greater than the 42° critical angle for AlSi10Mg. The geometry of this cell is shown in Figure 5a. The positioning and repetition within the wall are shown in Figure 5b.

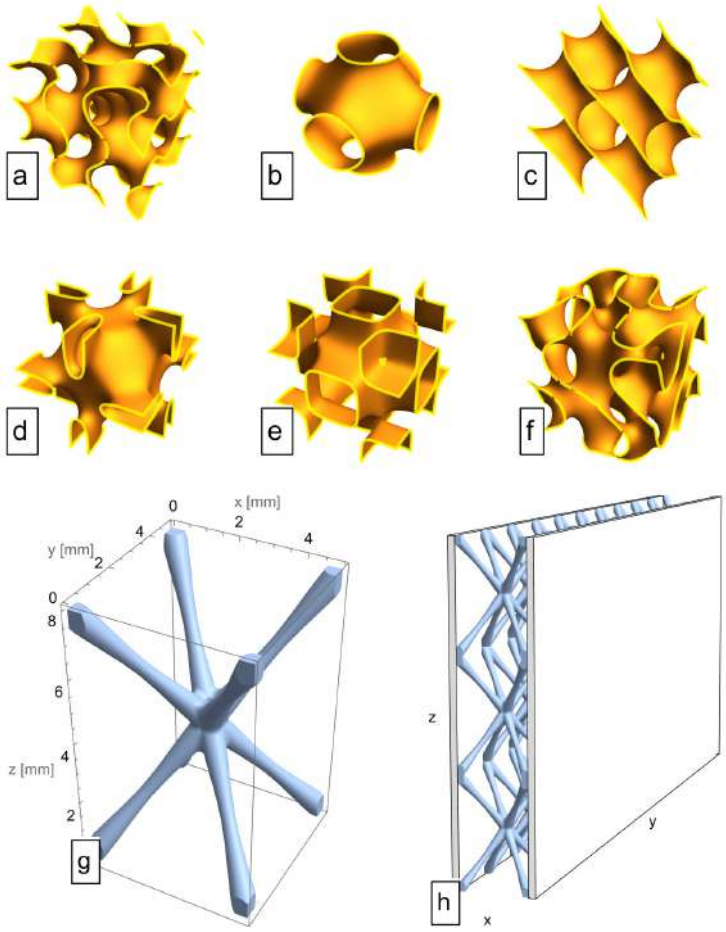

Figure 5. Investigated TPMS structures: Schwarz Gyroid (**a**), Primitive (**b**), Diamond (**c**), Nevious (**d**), Schoen I-WP (**e**), Fischer-Koch S Surface (**f**). Chosen lattice structure (**g**) and positioning within the wall (**h**).

Other cell sizes were selected considering bigger total wall thicknesses and beam dimensions. Later, the dynamic simulation will highlight that complying with the specification is the most challenging aspect of this work and many modifications will be required. In Table 4 the employed lattice types are reported. The total wall thickness is the sum

of the wall skin and the *x* dimension of the cell. It can be noticed that the lattice type B and D differ in the cell-to-wall joining: the latter showed better outcomes by means of structural rigidity.

Table 4. Lattice cell geometry.

	Lattice Dimensions				Minimum Overhanging Angle	Total Wall Thickness
	x	y	z	Beam		
Type	[mm]	[mm]	[mm]	[mm]	[°]	[mm]
A	5	5	8	0.4	48.5	5
B	10	10	16.5	0.85	49.4	11
C	20	10	25	1	48.2	21
D	11	11	16.5	0.9	46.7	11

Preliminary tests were carried out on these lattice types proving the fabricability of the small components and the module corner shown in Figure 6.

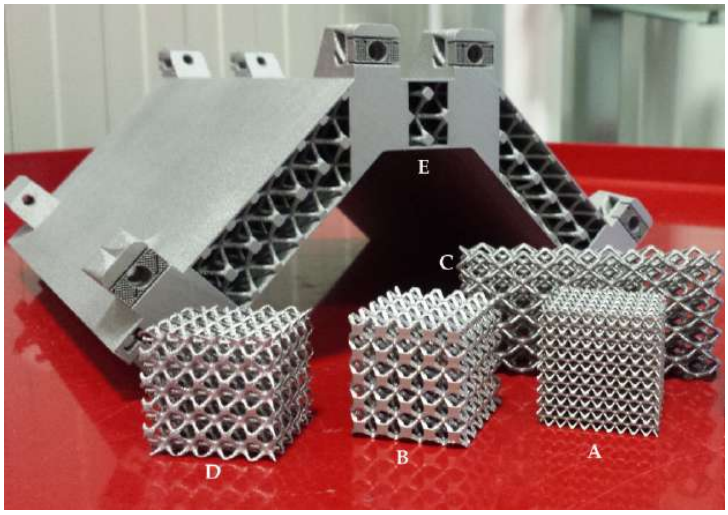

Figure 6. Manufacturability verification carried out on investigated cells: 5 × 5 × 8 (A), 10 × 10 × 16.5 (B), 20 × 10 × 25 (C), 11 × 11 × 16.5 (D) and prototype (E).

3.2. Thermal Plates

The module is characterized by many thermal plates (Figure 7). They are necessary to allow thermal communication between stacked structures. Their functional surface is perpendicular to the wall, hence they must be fabricated horizontally. The junction point wall is 25 × 11 × 1 mm^3 and requires a support structure inaccessible for removal in the post-processing.

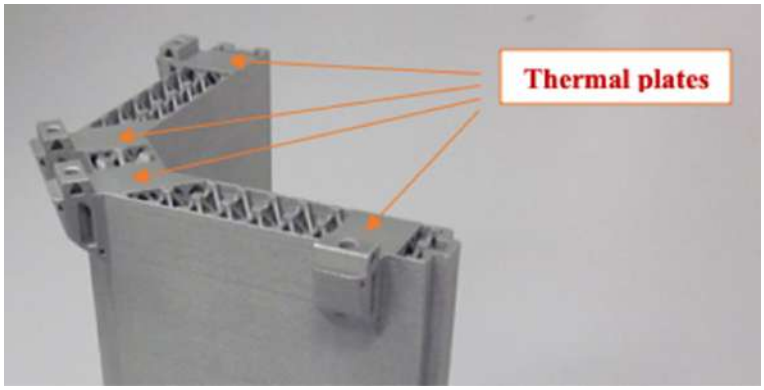

Figure 7. Thermal plates for allow the heat transfer between stacked structures.

To avoid this problem, the thermal plates were integrated in the lattice below designing the grow structure reported in Figure 8.

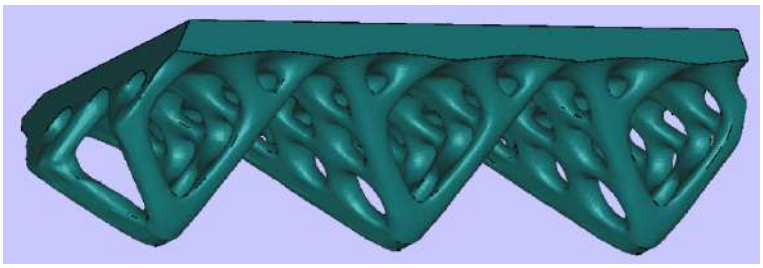

Figure 8. Self-supporting tree structure for upper thermal plates to overcome the problem of fabricating horizontal planes by PBF-LB/M.

3.3. Junction Points: Lightweighting

The original design of the junction points is based on traditional manufacturing technologies. They can be assimilated to parallelepipeds with threaded holes and machine-shaped joints (Figure 9a,b). To exploit the advantages of AM, an effective design strategy based on topology optimization was provided to generate lightweight designs for AM [60]. The upper junction joint was modified in order to have self-supporting surfaces and connected to its skin with a 3 mm-radius chamfer as shown in Figure 9c. The lower junction joint was lightened using gussets and reinforcing arms (Figure 9c).

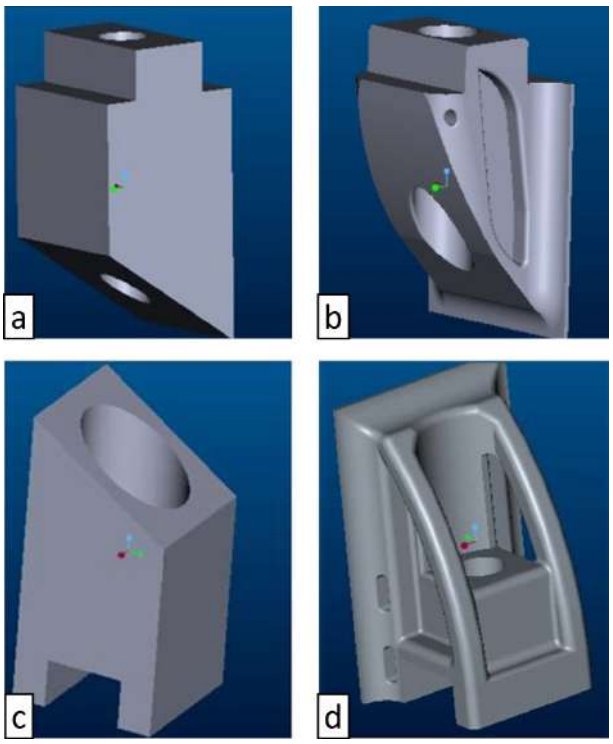

Figure 9. Original design (**a**) and AM redesign (**b**) of an upper junction point. Original design (**c**) and AM redesign (**d**) of a lower junction point.

The new design functionality was proven via Siemens PLM Femap® v11.3 simulation platform. The upper junction point (Figure 10a) showed a maximum Von Mises stress of 31 MPa at the bottom hole which is much lower than the fabricated material resistance. Minor values are reached at the wall connection. The lower junction point is more stressed by the local load as shown in Figure 10b: the reinforcing arms exhibit about 25 MPa at the top and nearby the hole housing; the maximum value of 79 MPa is observed at the

connection between the back plate and the hole housing. Additionally, for this junction point type, the simulation easily meets the requirements.

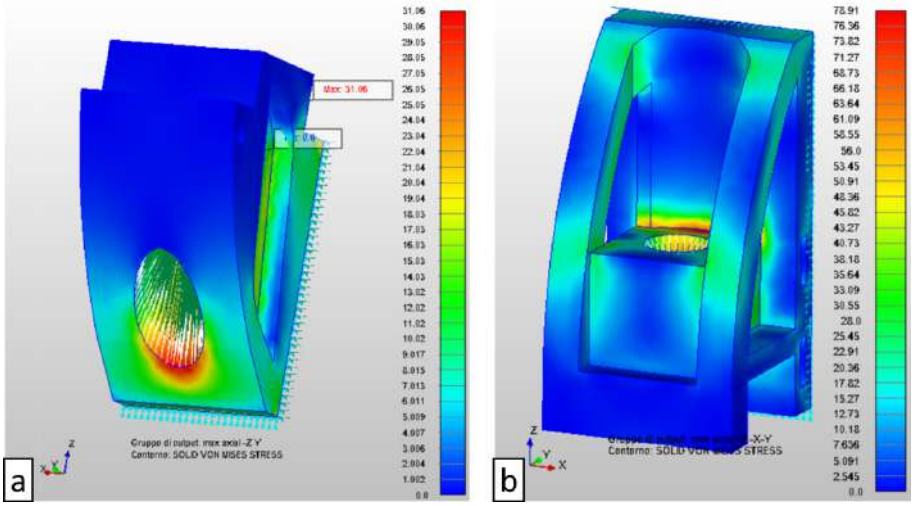

Figure 10. FEM simulation of the new upper (**a**) and lower (**b**) junction points.

3.4. Mechanical Properties and Allowable Values for AlSi10Mg

The parts were manufactured on a single laser EOS M400 printer. The choice of the single-laser model machine was made to reduce design risks typical of imperfect alignments in multi-laser systems. The mechanical properties for AlSi10Mg declared by EOS for a M400 single laser with a 90 µm layer thickness are shown in Table 5, with the heat-treated values referring to T6 heat treatment [61]. The decrease in the material's tensile strength, yield strength and elastic modulus after the heat treatment is due to microstructural coarsening: a reduction in grain boundary area limits the motion of the dislocation during deformation [62]. Conversely, an increase in ductility is obtained by thermal treatment, making this alloy more suitable for applications that require high ductility. The increase in grain size reduces the micro-hardness above all after the solution heat treatment which is partially recovered by a microstructure refinement in the T6 [63].

Table 5. AlSi10Mg mechanical properties.

Mechanical Characteristics	Unit	As Built	Heat-Treated
Tensile strength	MPa	410 ± 40	325 ± 20
Yield strength (Rp 0.2%)	MPa	240 ± 40	220 ± 20
Elongation at break	%	5 ± 2	9 ± 2
E-Modulus	GPa	65 ± 5	65 ± 5
Hardness (DIN EN ISO 6506-1)	HBW	120 ± 5	95 ± 5

A target value is necessary for the subsequent optimization process and must be chosen accordingly to a safety factor. The yield strength of 220 ± 20 MPa could suggest a value of 150 MPa resulting in a factor of 1.33 to take into account the relatively high variability.

However, the geometry of the trays is mainly composed of thin-wall structures, and cannot be subjected to the T6 treatment. A Stress Relieve treatment, consisting of annealing for 2 h at 300 °C, was chosen to minimize residual stresses from the PBF-LB/M process, thus modifying the obtainable material strength. A tensile test was performed to investigate this expected change. The test results for specimens placed vertically and horizontally with respect to the building platform are shown in Figure 11. The Young modulus was about 67 GPa with the highest variation in the vertical specimens. The thermal treatment allowed to increase the as-built elongation at break above all for the horizontal specimens. The measured tensile and yield strength were markedly reduced with respect to the T6 state.

This is not a surprising result since the used layer thickness of 90 µm is declared as having low Technology Readiness Level by EOS GmbH. The yield strength, in particular, was about 167 MPa. Thus, in order to have a margin of safety the target value for the optimization was considered equal to 130 MPa.

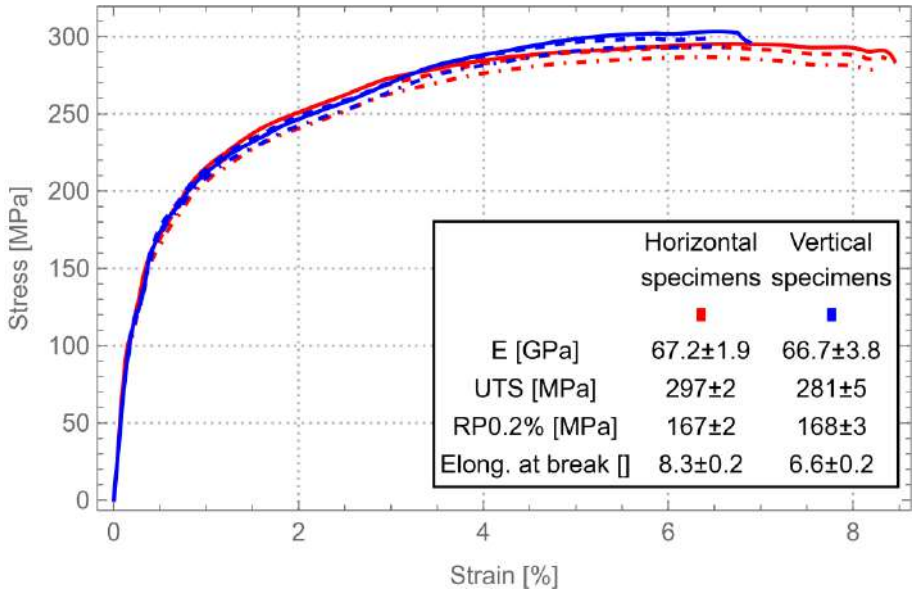

Figure 11. AlSi10Mg σ-ε curve for horizontal and vertical specimens, after Stress Relieving.

3.5. Design Optimization-Structural Loads

All the analyses and verifications including model preparation were made using the software Within® (Autodesk®, San Francisco, CA, USA) FEMAP® (Siemens PLM Software, Plano, TX, USA) and the solver Nastran® 2016 (Autodesk®, San Francisco, CA, USA).

In the design attempts many fails came from the balancing of the mass and the satisfaction of the dynamic requirements as will be clear in the following Section 3.6. Thus, a new optimization method was introduced in order to reduce the Von Mises stress to a minimum value by locally thickening those elements requiring more stiffness. For this purpose, the framework reported in Figure 12 was developed. Each module was designed in Autodesk® Within® by selecting the total thickness and adding all the necessary elements, namely the thermal plates, the upper, the lower and the wall junctions. For several lattice structures, the cell was defined by changing the dimensions and the wall skin thickness. Finally, the lattice geometry is generated only in selected regions.

The geometry is loaded in Autodesk® Nastran 2016 Solver. For each structural load (ref. Table 4), the boundary conditions are given and a static analysis calculating Von Mises stress is provided. A thickening is applied to those regions exceeding the maximum value and a new geometry is generated. Based on the previous analysis this value was set at 130 MPa. The loop stops when all the regions satisfy the requirements. Figure 13a shows a local thickening applied to the zone between the upper junctions at the module corner. After generating the geometry, the module is subjected to a linear buckling analysis and a linear buckling safety factor is calculated. This verification allows establishing if the structure is subjected to buckling instability under the specified boundary conditions.

If the factor is less than 1 the thickening value is increased, and a new thickening is applied to the previously modified regions. A new static analysis is provided, and the loop is repeated until a geometry satisfying the safety factor is created. As a result, the original regular lattice structure is transformed into an uneven pattern as shown in Figure 13b.

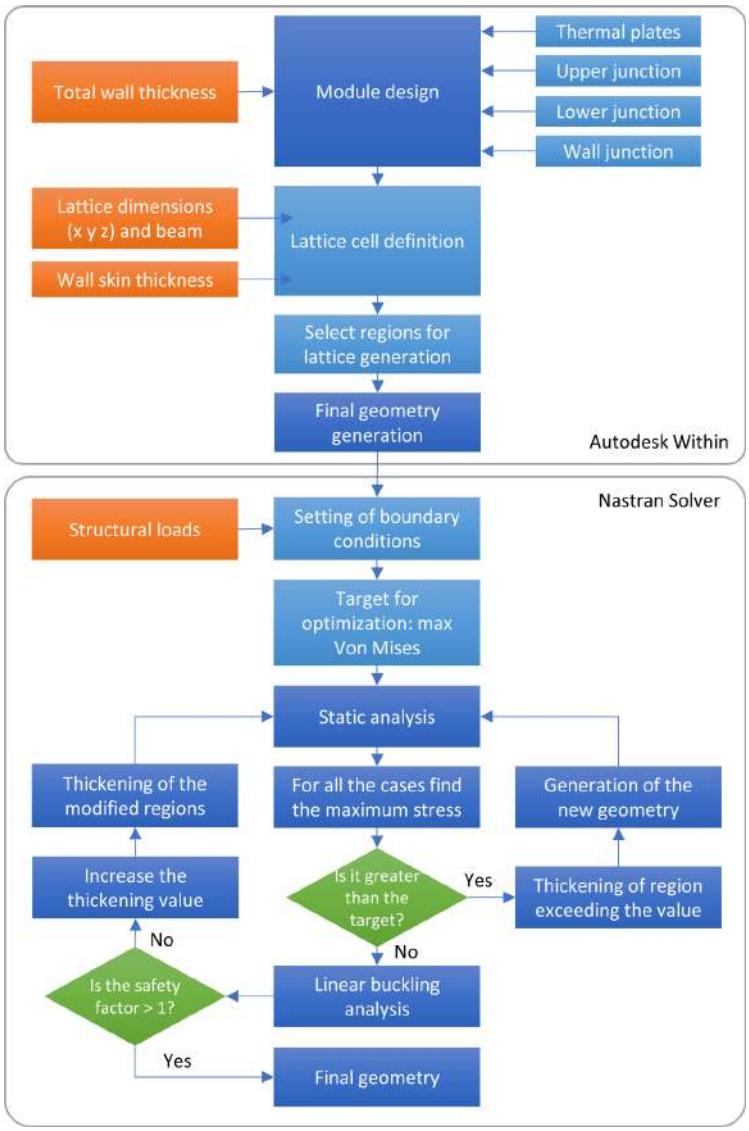

Figure 12. Lattice structures optimization design framework.

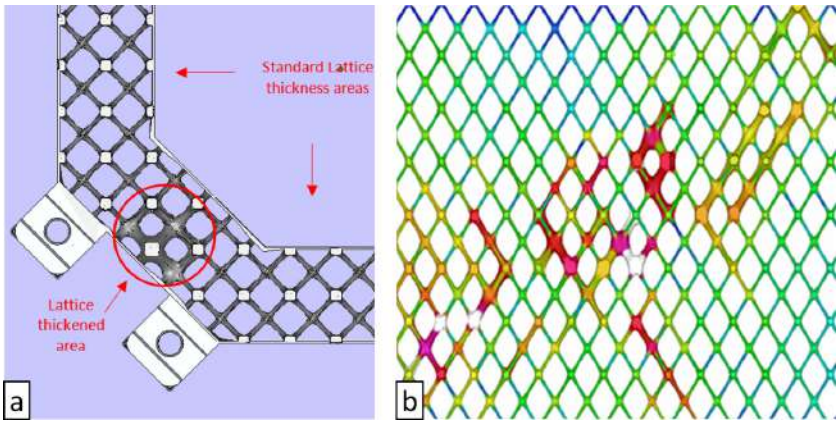

Figure 13. Example of local thickening (**a**) and multiple pass thickening (**b**).

3.6. Modal Analysis

Modal analyses were performed on both modules in order to verify that their optimized design meets the stiffness requirements. The models were prepared through the

Siemens PLM Software pre-processor Femap v11.3. The solver used for the analyses is Autodesk® Nastran® 2016. Table 6 shows the original design as well as many attempts and the outcomes of the dynamic simulation in terms of natural frequencies. Particular attention was paid to the Young modulus used in the simulation since the experimental investigations claimed values smaller than the declared one.

Table 6. Modal analyses and weights for investigated lattice structures.

ID	Total Wall Thickness	Wall Skin Thickness	Lattice Element					E	Bonding Walls	Optimized Design	Natural Frequencies			Panel 100 × 100 mm²	
			Type	x	y	z	Beam				I	II	III	Weight	Weight
				[mm]	[mm]	[mm]	[mm]	[Gpa]			[Hz]	[Hz]	[Hz]	[g]	%
0	5	full	-	-	-	-	-	74	no	no	23	24	144	58.3	100.00
1	5	0.5	A	5	5	8	0.4	67	no	no	37	39	221	35.14	60.27
2	5	0.5	A	5	5	8	0.4	74	no	no	39	41	232	35.14	60.27
3	21	0.5	B	10	10	16.5	0.85	74	no	no	47	47	212	66.93	114.80
4	11	0.5	C	20	10	25	1	67	yes	no	34	35	216	41.43	71.06
5	11	0.5	C	20	10	25	1	74	yes	no	36	37	227	41.43	71.06
6	11	0.5	D	11	11	16.5	0.9	67	yes	no	38	39	231	46.97	80.57
7	11	0.5	D	11	11	16.5	0.9	60	yes	no	36	37	218	46.97	80.57
8	11	1	D	11	11	16.5	0.9	67	yes	no	67	90	283	73.47	126.02
9	11	0.5	D	11	11	16.5	0.9	67	yes	yes	48	50	254	47.6	81.65
10	11	0.5	D	11	11	16.5	0.9	60	yes	yes	46	48	240	47.6	81.65

The original design (ID 0) considers an aluminum alloy characterized by a 74 GPa Young modulus. Nevertheless, the first natural frequency is 23 Hz, much less than the requested one. The weight of a 100 × 100 mm^2 panel of this configuration weighs 58.3 g. This value is taken as a reference for comparison with the proposed designs.

The first structure was selected to maintain the original total wall thickness: a 5 × 5 × 8 mm^3 cell characterized by a 0.4 mm beam was simulated considering 67 GPa and 74 GPa (ID 1 and 2, respectively). The first frequency was borderline although the weight saving was impressive. A 10 × 10 × 17 mm^3 was chosen for ID 3: in this case, two cells form the total wall thickness which was increased to 21 mm. The first frequency was not satisfying the specification, but the weight was bigger than the original. Thus, the wall thickness was reduced to 11 mm and a 20 × 10 × 25 mm^3 was selected. In this configuration, the EOS M400 building limitation is considered and the module was subdivided into four parts. As a consequence, the walls were simulated considering the bonding of the walls on joining surfaces. These modifications added weight and reduced stiffness. This solution is good for weight saving but the first frequency returned below the admissible limit for 67 GPa modulus (ID 4). The simulation employing 74 GPa modulus (ID 5) evidenced that the effect on the natural frequency is limited, and this cell cannot be effectively used. A better result was given by using an 11 × 11 × 17 mm^3 cell structure at 67 GPa modulus (ID 6). The weight saving, in this case, is about 20%. Since the results obtained by this material were in terms of rigidity, a lower modulus value was simulated in ID 7 evidencing a result just 2 Hz below the frequency request. Till now the wall skin thickness was maintained at 0.5 mm for weight saving. More stiffness is expected for increased thickness. The simulation ID 8 considers 1 mm skin thickness and the same lattice cell. The first natural frequency is now 67 but the weight is 26% more than the original. At this point, the previous configuration was subjected to the optimized design framework. The weight was marginally affected, allowing for more than 18% saving with respect to the original design. The first natural frequency was 48 Hz (ID 9) and 46 Hz (ID 10) at 67 GPa and 60 GPa, respectively.

The previous analysis can be summarized by the graph in Figure 14. The green area represents the desired zone where the weight of the module does not exceed the original one and its first natural frequency is higher than the minimum admissible value. It is evident how it is easy to comply with the dynamic requirements by providing a big wall thickness (ST1) or a large structure (WT21) to the detriment of the total weight. A very small structure (WT5) is very light but too close to the frequency limit. A wall thickness of

11 mm is an interesting configuration (WT11). The cell type C (ID 4 and 5) does not satisfy the requirements. Conversely, cell type D is promising and by using an optimized design it is possible to have a good choice in terms of light structure and dynamic response. This last design will be adopted for fabrication and experimental validation.

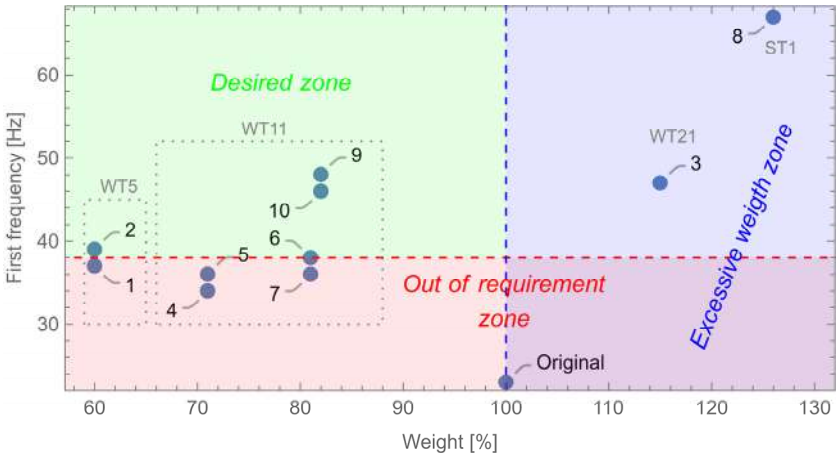

Figure 14. Investigated lattice structure modal analysis results versus panel weight.

4. Fabrication and Validation

The solution of the optimized design was selected for physical prototyping by using an EOS M400. In Figure 15a the component after the exceeding powder removal and before the detachment from the building platform is shown. The cutting and the support structure removal were provided with care and a manual assembly made use of the jig as reported in Figure 15b. This configuration was used as a fixturing system for the machining of the additional material (Figure 15c).

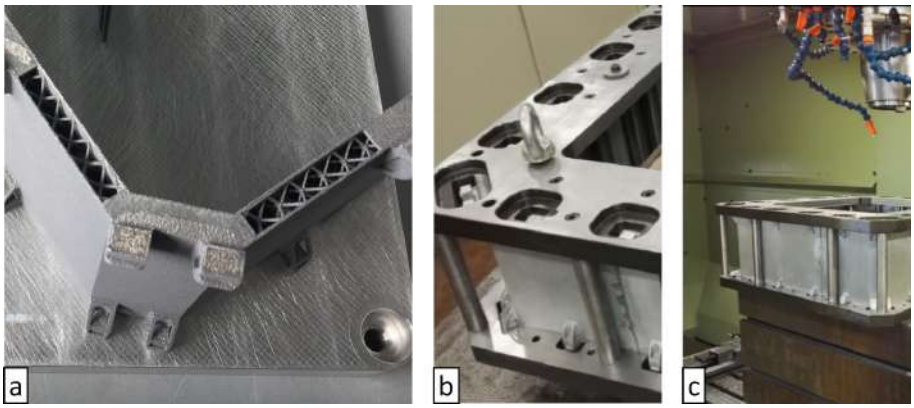

Figure 15. Fabricated component (**a**), assembly within the jig (**b**), machining (**c**).

The most time-consuming operation is the PBF-LB/M fabrication as evidenced in Table 7. The AM step requires 53% of the total time. Particular care was paid to the CNC removal of the additional material which took 44 h accounting for 28% of the total time. Additionally, it is relevant to note that the AM fabrication is automatic after setting up the system, hence it required 4 days as well as the CNC machining that was undertaken during a normal working shift. The traditional machining of the original design is also reported for comparison. The aluminum solid stock is firstly cut by wire EDM and a stress-relieving heat treatment follows. The CNC strategy is roughing, pocketing for the inside of each area surrounded by the ribs, and finishing. As expected, a very long time is required for pocketing and finishing since the forces must be kept very low for avoiding deformations of the thin walls [64]. These long processing times highlight that the satellite

structure is expensive if compared with serial production via traditional technology. It is noteworthy that the structure, in this case, is simplified to allow the tool accessibility and functionality can be reduced or compromised as in the present case where the natural frequency specification was not accomplished. When complex and low-mass parts are produced, the AM becomes competitive and can enable the possibility to fabricate high-performance structures allowing relevant cost-saving in space missions at different levels.

Table 7. Processing time for the various realization steps.

Process	PBF-LB/M Fabrication (EOS M400)	Heat Treatment	EDM Cutting	Assembly in the Jig	CNC Machining	Testing
Time [h]	84	7	4	4	44	16
Process	EDM cutting of the stock	Heat treatment	CNC roughing	CNC pocketing	CNC finishing	Testing
Time [h]	11	6	23	40	32	16

The machined component was subjected to tolerance verification. In Figure 16 the dimensions and required tolerances are shown. The measured ones are indicated in green.

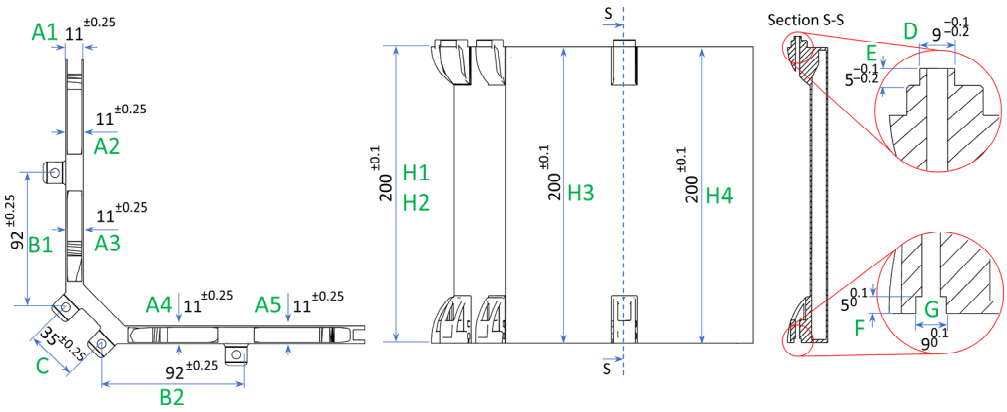

Figure 16. Component dimensions and tolerances and measured zones (in green).

Table 8 reports the outcomes of the analysis. The total wall thickness is within the requested range and shows only positive deviations, hence, a slightly bigger weight than the designed one is expected. The distances between the junction points vary within a few hundred mm, widely meeting the requested ±0.25 mm. Analogously, all the measures are taken on the component height range within ±0.05 mm. An important role is played by the junction point mating pit and tooth shown in section S-S in Figure 16. Additionally, for these features the required limits are satisfied demonstrating the possibility to use the manufacturing coupling between AM and CNC to provide an in-tolerance satellite structure.

A microstructural analysis was performed on the fabricated component. Surfaces were cut by Struers® Labotom 6, polished by a Struers® Labopol and etched with Weck's reagent. The vertical wall shows a typical microstructure evidencing the contour and hatching laser strategies (Figure 17a) [55]. Partially superimposed melt pools are well evident as typical for this AM technology. A little defect can be noticed in the contour zone: the rounded shape can suggest it depends upon a trapped gas, probably due to some inefficiencies of the protective flow [65,66]. Indeed, big machines such as the EOS M400 suffer from uniform gas distribution which may affect the powder bed development of this light alloy. Figure 17b shows the section on the lattice structure: the contour and hatch zone can be identified; also in this case, a small defect is present. The examination at higher magnification (Figure 17c) highlights that the cellular structure grows in the direction of the cooling which is very high

at the boundary of the melt pool [43]. In this area, the structure is dendritic as expected for a solidifying metallic alloy. Moving to the center the microstructure changes and becomes uniform [42]. Figure 17d points out this difference: the left zone of the image is taken on the melt pool boundary and shows a dendritic growth from the left to the right; elsewhere very fine grains can be observed.

Table 8. Dimensional verification of fabricated components.

	Dimension					In Tolerance
Element	**Nominal**	**Measured**	**Deviation**	**Negative**	**Positive**	
A1	11	11.1	0.1	−0.25	0.25	Yes
A2	11	11.07	0.07	−0.25	0.25	Yes
A3	11	11.04	0.04	−0.25	0.25	Yes
A4	11	11.09	0.09	−0.25	0.25	Yes
B1	92	92.03	0.03	−0.25	0.25	Yes
B2	92	91.98	−0.02	−0.25	0.25	Yes
C	35	35.04	0.04	−0.25	0.25	Yes
H1	200	200.05	0.05	−0.1	0.1	Yes
H2	200	200.02	0.02	−0.1	0.1	Yes
H3	200	199.96	−0.04	−0.1	0.1	Yes
H4	200	200.03	0.03	−0.1	0.1	Yes
D1	9	8.87	−0.13	−0.2	−0.1	Yes
E1	5	4.85	−0.15	−0.2	−0.1	Yes
F1	9	9.02	0.02	0	0.1	Yes
G1	5	5.05	0.05	0	0.1	Yes
D2	9	8.85	−0.15	−0.2	−0.1	Yes
E2	5	4.89	−0.11	−0.2	−0.1	Yes
F2	9	9.06	0.06	0	0.1	Yes
G2	5	5.02	0.02	0	0.1	Yes
D3	9	8.88	−0.12	−0.2	−0.1	Yes
E3	5	4.84	−0.16	−0.2	−0.1	Yes
F3	9	9.03	0.03	0	0.1	Yes
G3	5	5.05	0.05	0	0.1	Yes
D4	9	8.84	−0.16	−0.2	−0.1	Yes
E4	5	4.85	−0.15	−0.2	−0.1	Yes
F4	9	9.03	0.03	0	0.1	Yes
G4	5	5.04	0.04	0	0.1	Yes

The fabricated and assembled module was submitted to a load test according to the module specification. The module was assembled into two plates by using the junction points. The upper plate is characterized by a flanged rod in order to apply load case 1 as shown in Figure 18a. The test was carried out in an MTS model C43 universal test machine in two configurations: for the compression, the load was applied directly to the rod (Figure 18b); the lateral load was applied by using a socket on a rod with the structure rotated by 90° and fixtured by an L bracket (Figure 18c). For both cases, the speed was chosen at 1 mm/s till the load is reached and no extensometer was used. The result of the test confirmed the capability to resist the requested static loads.

Finally, the weight of each module was measured and reported in Table 9.

Table 9. Prototype mass comparison.

	Final Weight	**Estimated Weight**	**Variation**	**Original Weight**	**Final Mass Saving**	**Estimated Mass Saving**
	[kg]	**[kg]**	**[kg]**	**[kg]**	**[%]**	**[%]**
Module 1	2.70	2.66	+0.04	2.78	−1.03	−4.31
Module 2	4.10	3.80	+0.30	5.26	−22.05	−27.76
Total	6.80	6.46	+0.34	8.04	−18.24	−19.62

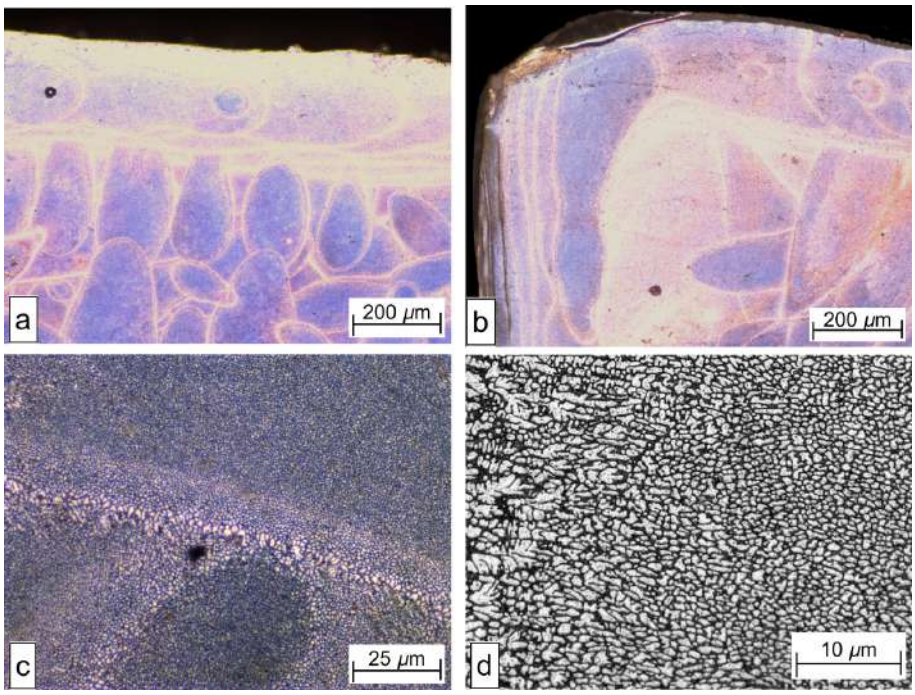

Figure 17. Micrographs of the module wall (**a**), the lattice structure (**b**), the melt pool boundary (**c**), grain microstructure (**d**).

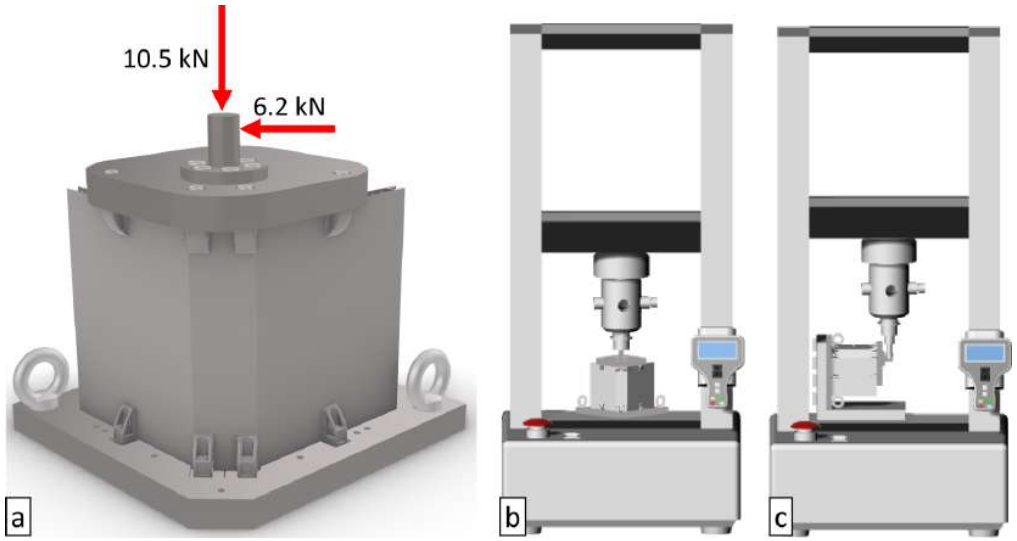

Figure 18. Schematic module assembly for of the static verification system (**a**), compression (**b**) and lateral load (**c**) configuration.

It can be observed that the obtained masses are higher than the estimations. The exceeding mass in each module has been associated with two main factors:

- Non-optimal Beam Offset calibration of the PBF-LB/M process. This machine parameter is associated with the geometrical correction of each section to compensate for the geometry of the laser spot;
- CNC milling. During this step, the milling operation had to compensate for small deformations of the 3D-printed components. Therefore, in some areas slightly less material has been subtracted with respect to what has been planned originally in order to comply with dimensional tolerances (max 0.1 mm) and minimum wall thickness (0.5 mm).

5. Conclusions

This work presents an integrated redesign of a module that is part of a satellite platform employing PBF-LB/M and lattice structure. The method considers all the fabrication steps and provides a selection for lattice structures as well as the skin. The final design includes features that can be manufactured only by AM technologies. The following conclusions can be drawn:

- The proposed design optimization allowed us to find a solution complying with the first frequency request which was not satisfied by the original design fabricated via traditional manufacturing.
- The selected fabrication parameters, in particular the high layer thickness, allow a fast fabrication. However, the resulting strength is lower than expected for this Aluminum alloy. Furthermore, it is lowered by the thermal treatment selected for the lattice structure cares.
- The modal analysis demonstrated that satisfying the frequency requirement is most challenging if a lightweight structure must be attained. For this purpose, a particular framework was developed and adopted for locally thickening the critical zones of the lattice. The adoption of a particular cell complied with the specification with a good margin also in the case where the simulation was provided with a very low Young modulus value.
- The total estimated weights of the parts are 2.66 Kg for Module 1 and 3.8 Kg for Module 2, that lead to a weight saving, respectively, equal to 0.12 Kg (4.3%) and 1.46 Kg (27.8%).

Author Contributions: Conceptualization, L.M. and A.B.; methodology, A.B. and L.B.; software, L.M.; validation, A.B.; formal analysis, A.B.; investigation, L.B.; resources, L.M.; data curation, L.B.; writing—original draft preparation, S.V. and L.B.; writing—review and editing, A.B. and L.B.; visualization, S.V.; supervision, A.B. and L.M.; project administration, L.M.; funding acquisition, L.M. All authors have read and agreed to the published version of the manuscript.

Funding: This research received no external funding.

Institutional Review Board Statement: Not applicable.

Informed Consent Statement: Not applicable.

Data Availability Statement: Not applicable here.

Acknowledgments: The authors would like to thank Paolo Marconato, Paolo Volpe, Michele Fornasiero and Cristina Necula, for their help and effort in designing and prototyping this challenging project.

Conflicts of Interest: The authors declare no conflict of interest.

References

1. Kopacz, J.R.; Herschitz, R.; Roney, J. Small satellites an overview and assessment. *Acta Astronaut.* **2020**, *170*, 93–105. [CrossRef]
2. Millan, R.M.; Von Steiger, R.; Ariel, M.; Bartalev, S.; Borgeaud, M.; Campagnola, S.; Castillo-Rogez, J.C.; Fléron, R.; Gass, V.; Gregorio, A.; et al. Small satellites for space science A COSPAR scientific roadmap. *Adv. Space Res.* **2019**, *64*, 1466–1517. [CrossRef]
3. Lappas, V.; Kostopoulos, V. A Survey on Small Satellite Technologies and Space Missions for Geodetic Applications. In *Satellites Missions and Technologies for Geosciences*; Demyanov, V., Becedas, J., Eds.; IntechOpen: London, UK, 2020.
4. Camps, A. Nanosatellites and Applications to Commercial and Scientific Missions. In *Satellites Missions and Technologies for Geosciences*; Demyanov, V., Becedas, J., Eds.; IntechOpen: London, UK, 2019.
5. Bryce and Space Technology. SmallSat by the Numbers. 2021. Available online: https://brycetech.com/reports (accessed on 29 January 2023).
6. Nguyen, H.; Nguyen, P. Communication Subsystems for Satellite Design. In *Satellite Systems*; Nguyen, T.M., Ed.; IntechOpen: London, UK, 2020.
7. SpaceX Falcon User Guide. 2021. Available online: https://www.spacex.com/media/falcon-users-guide-2021-09.pdf (accessed on 29 January 2023).
8. Pérez, A.G.; Sanz-Andrés, A. Dynamic coupling on the design of space structures. *Aerosp. Sci. Technol.* **2019**, *84*, 1035–1048. [CrossRef]

9. NASA. State-of-the-Art of Small Spacecraft Technology. 2021. Available online: https://www.nasa.gov/smallsat-institute/sst-soa/ (accessed on 29 January 2023).
10. Moog Has Shipped the Satellite Dispenser to Cape Canaveral Air Force Station to support ORBCOMM Generation 2 Satellites. 2015. Available online: https://www.moog.com/news/operating-group-news/2015/moog-has-shipped-the-satellite-dispense (accessed on 29 January 2023).
11. Laufer, R.; Pelton, J.N. The Smallest Classes of Small Satellites Including Femtosats, Picosats, Nanosats, and CubeSats. In *Handbook of Small Satellites*; Springer: Cham, Switzerland, 2019; pp. 1–15.
12. Ariannespace SSMS Vega C Users Manual. 2020. Available online: https://www.arianespace.com/wp-content/uploads/2020/10/SSMS-Vega-C-UsersManual-Issue-1-Rev0-Sept2020.pdf (accessed on 29 January 2023).
13. Blakey-Milner, B.; Gradl, P.; Snedden, G.; Brooks, M.; Pitot, J.; Lopez, E.; Leary, M.; Berto, F.; du Plessis, A. Metal additive manufacturing in aerospace: A review. *Mater. Des.* **2021**, *209*, 110008. [CrossRef]
14. Boyer, R.; Cotton, J.; Mohaghegh, M.; Schafrik, R. Materials considerations for aerospace applications. *MRS Bull.* **2015**, *40*, 1055–1066. [CrossRef]
15. Najmon, J.C.; Raeisi, S.; Tovar, A. Review of additive manufacturing technologies and applications in the aerospace industry. In *Additive Manufacturing for the Aerospace Industry*; Elsevier: Amsterdam, The Netherlands, 2019; pp. 7–31.
16. Gibson, I.; Rosen, D.W.; Stucker, B. *Additive Manufacturing Technologies*; Springer: New York, NY, USA, 2021.
17. Westerweel, B.; Basten, R.J.; Van Houtum, G.J. Traditional or Additive Manufacturing? Assessing Component Design Options through Lifecycle Cost Analysis. *Eur. J. Oper. Res.* **2018**, *2270*, 570–585. [CrossRef]
18. Kerstens, F.; Cervone, A.; Gradl, P. End to end process evaluation for additively manufactured liquid rocket engine thrust chambers. *Acta Astronaut.* **2021**, *182*, 454–465. [CrossRef]
19. Kumar, L.J.; Krishnadas Nair, C.G. Current Trends of Additive Manufacturing in the Aerospace Industry. In *Advances in 3D Printing & Additive Manufacturing Technologies*; Springer: Singapore, 2016; pp. 39–54.
20. Fores, F.; Boyer, R. *Additive Manufacturing for the Aerospace Industry*, 1st ed.; Elsevier: Amsterdam, The Netherlands, 2019.
21. Shapiro, A.A.; Borgonia, J.P.; Chen, Q.N.; Dillon, R.P.; McEnerney, B.; Polit-Casillas, R.; Soloway, L. Additive Manufacturing for Aerospace Flight Applications. *Spacecr. Rocket.* **2016**, *53*, 952–959. [CrossRef]
22. Samal, S.K.; Vishwanatha, H.M.; Saxena, K.K.; Behera, A.; Nguyen, T.A.; Behera, A.; Prakash, C.; Dixit, S.; Mohammed, K.A. 3D-Printed Satellite Brackets: Materials, Manufacturing and Applications. *Crystals* **2022**, *12*, 1148. [CrossRef]
23. nTopology. Case Study: US Air Force Optimizes CubeSat Using Architected Materials. 2022. Available online: https://ntopology.com/resources/download-case-study-summary-cubesat/ (accessed on 29 January 2023).
24. Debnath, B.; Shakur, M.S.; Tanjum, F.; Rahman, M.A.; Adnan, Z.H. Impact of Additive Manufacturing on the Supply Chain of Aerospace Spare Parts Industry—A Review. *Logistics* **2022**, *6*, 28. [CrossRef]
25. Yang, S.; Tang, Y.; Zhao, Y.F. A new part consolidation method to embrace the design freedom of additive manufacturing. *J. Manuf. Process.* **2015**, *20*, 444–449. [CrossRef]
26. Boschetto, A.; Bottini, L.; Eugeni, M.; Cardini, V.; Graterol Nisi, G.; Veniali, F.; Gaudenzi, P. Selective Laser Melting of a 1U CubeSat structure. Design for Additive Manufacturing and assembly. *Acta Astronaut.* **2019**, *159*, 377–384. [CrossRef]
27. Boschetto, A.; Bottini, L.; Cardini, V.; Eugeni, M.; Gaudenzi, P.; Veniali, F. Aircraft part substitution via additive manufacturing: Design, simulation, fabrication and testing. *Rapid Prototyp. J.* **2021**, *27*, 995–1009. [CrossRef]
28. An Epiphany of Disruption: GE Additive Chief Explains How 3D Printing Will Upend Manufacturing GE News. 2022. Available online: https://www.ge.com/news/reports/epiphany-disruption-ge-additive-chief-explains-3d-printing-will-upend-man (accessed on 3 November 2022).
29. GE Additive. 2021. Available online: https://www.ge.com/additive/additive-parts (accessed on 3 November 2022).
30. Yan, C.; Hao, L.; Hussein, A.; Raymont, D. Evaluations of cellular lattice structures manufactured using selective laser melting. *Int. J. Mach. Tools Manuf.* **2012**, *62*, 32–38. [CrossRef]
31. Xu, S.; Shen, J.; Zhou, S.; Huang, X.; Xie, Y.M. Design of lattice structures with controlled anisotropy. *Mater Des.* **2016**, *93*, 443–447. [CrossRef]
32. Scaccabarozzi, D.; Biffi, C.A.; Saggin, B.; Magni, M.; Valnegri, P.; Fiocchi, J.; Tuissi, A. Design and testing of selective laser melted structural component in AlSi9Cu3 alloy for a space dust analyser. *Acta Astronaut.* **2021**, *184*, 193–207. [CrossRef]
33. Zhang, X.; Zhou, H.; Shi, W.; Zeng, F.; Zeng, H.; Chen, G. Vibration Tests of 3D Printed Satellite Structure Made of Lattice Sandwich Panels. *AIAA J.* **2018**, *56*, 4213–42178. [CrossRef]
34. Zhou, H.; Jia, H.; Zeng, H.; Tu, Y.; Li, L.; Zhang, X.; Lei, H. Resonance frequency prediction approach of lattice structure fabricated by selective laser melting. *Adv. Astronaut. Sci. Technol.* **2022**, *5*, 309–316. [CrossRef]
35. Jia, D.; Li, F.; Zhang, Y. 3D-printing process design of lattice compressor impeller based on residual stress and deformation. *Sci. Rep.* **2020**, *10*, 600. [CrossRef]
36. Zhou, H.; Zhang, X.; Zeng, H.; Yang, H.; Lei, H.; Li, X.; Wang, Y. Lightweight structure of a phase-change thermal controller based on lattice cells manufactured by SLM. *Chin. J. Aeronaut.* **2019**, *32*, 1727–1732. [CrossRef]
37. Song, B.; Zhao, X.; Li, S.; Han, C.; Wei, Q.; Wen, S.; Liu, J.; Shi, Y. Differences in microstructure and properties between selective laser melting and traditional manufacturing for fabrication of metal parts: A review. *Front. Mech. Eng.* **2015**, *10*, 111–125. [CrossRef]

38. Zhang, J.; Song, B.; Wei, Q.; Bourell, D.; Shi, Y. A review of selective laser melting of aluminum alloys: Processing, microstructure, property and developing trends. *J. Mater. Sci. Technol.* **2019**, *35*, 270–284. [CrossRef]
39. He, L.; Kang, J.; Huang, T.; Rong, K. The integrated technique for the heat treatment of aluminium-alloy castings: A review. *Heat Treat. Met.* **2004**, *31*, 69–72.
40. Yan, Q.; Song, B.; Shi, Y. Comparative study of performance comparison of AlSi10Mg alloy prepared by selective laser melting and casting. *J. Mater. Sci. Technol.* **2020**, *41*, 199–208. [CrossRef]
41. Asgari, H.; Baxter, C.; Hosseinkhani, K.; Mohammadi, M. On microstructure and mechanical properties of additively manufactured AlSi10Mg_200C using recycled powder. *Mater. Sci. Eng. A* **2017**, *707*, 148–158. [CrossRef]
42. Aboulkhair, T.N.; Simonelli, M.; Parry, L.; Ashcroft, I.; Tuck, C.; Hague, R. 3D printing of Aluminium alloys: Additive Manufacturing of Aluminium alloys using selective laser melting. *Prog. Mater. Sci.* **2019**, *106*, 100578. [CrossRef]
43. Trevisan, F.; Calignano, F.; Lorusso, M.; Pakkanen, J.; Aversa, A.; Ambrosio, E.P.; Lombardi, M.; Fino, P.; Manfredi, D. On the Selective Laser Melting (SLM) of the AlSi10Mg Alloy: Process, Microstructure, and Mechanical Properties. *Materials* **2017**, *10*, 76. [CrossRef]
44. Beretta, S.; Romano, S. A comparison of fatigue strength sensitivity to defects for materials manufactured by AM or traditional processes. *Int. J. Fatigue* **2017**, *94*, 178–191. [CrossRef]
45. Maamoun, A.H.; Xue, Y.F.; Elbestawi, M.A.; Veldhuis, S.C. Effect of Selective Laser Melting Process Parameters on the Quality of Al Alloy Parts: Powder Characterization, Density, Surface Roughness, and Dimensional Accuracy. *Materials* **2018**, *11*, 2343. [CrossRef]
46. Gumbleton, R.; Cuenca, J.A.; Klemencic, G.M.; Jones, N.; Porch, A. Evaluating the coefficient of thermal expansion of additive manufactured AlSi10Mg using microwave techniques. *Addit. Manuf.* **2019**, *30*, 100841. [CrossRef]
47. Venettacci, S.; Ponticelli, G.S.; Guarino, D.; Guarino, S. Tribological properties of Laser Powder Bed Fused AlSi10Mg: Experimental study and statistical analysis. *J. Manuf. Process.* **2022**, *84*, 1103–1121. [CrossRef]
48. Zeynali, O.; Masti, D.; Gandomkar, S. Shielding protection of electronic circuits against radiation effects of space high energy particles. *Adv. Appl. Sci. Res.* **2012**, *3*, 446–451.
49. Korkmaz, M.E.; Gupta, M.K.; Robak, G.; Moj, K.; Krolczyk, G.M.; Kuntoğlu, M. Development of lattice structure with selective laser melting process: A state of the art on properties, future trends and challenges. *Manuf. Process.* **2022**, *81*, 1040–1063. [CrossRef]
50. Yongxin, G.; Lihua, Z.; Zhijia, L.; Yimin, G.; Lingxi, M. Optimization Design of Star Tracker Bracket of Small Satellite for 3D Printing. In Proceedings of the 2019 5th International Conference on Control, Automation and Robotics (ICCAR), Beijing, China, 19–22 April 2019.
51. Caiazzo, F.; Alfieri, V.; Fabbricatore, A.; Argenio, P. Topological optimization and additive manufacturing of a metal functional panel for multi-mission modular satellite platform. In Proceedings of the IEEE 9th International Workshop on Metrology for AeroSpace (MetroAeroSpace), Pisa, Italy, 27–29 June 2022.
52. Boschetto, A.; Bottini, L.; Pilone, D. Effect of laser remelting on surface roughness and microstructure of AlSi10Mg selective laser melting manufactured parts. *Int. J. Adv. Manuf. Technol.* **2021**, *113*, 2739–2759. [CrossRef]
53. Praneeth, J.; Venkatesh, S.; Krishna, L.S. Process parameters influence on mechanical properties of AlSi10Mg by SLM. *Mater. Today Proc.* **2023**, in press. [CrossRef]
54. Pfaff, A.; Jäcklein, M.; Schlager, M.; Harwick, W.; Hoschke, K.; Balle, F. An Empirical Approach for the Development of Process Parameters for Laser Powder Bed Fusion. *Materials* **2020**, *13*, 5400. [CrossRef] [PubMed]
55. Yadroitsev, I.; Yadroitsava, I.; Du Plessis, A.; MacDonald, E. *Fundamentals of Laser Powder Bed Fusion of Metals*, 1st ed.; Elsevier: Amsterdam, The Netherlands, 2021.
56. Read, N.; Wang, W.; Essa, K.; Attallah, M.M. Selective laser melting of AlSi10Mg alloy: Process optimization and mechanical properties development. *Mater. Des* **2015**, *65*, 417–424. [CrossRef]
57. Feng, J.; Fu, J.; Yao, X.; He, Y. Triply periodic minimal surface (TPMS) porous structures: From multi-scale design, precise additive manufacturing to multidisciplinary applications. *Int. J. Extrem. Manuf.* **2022**, *4*, 022001. [CrossRef]
58. Maconachie, T.; Leary, M.; Lozanovski, B.; Zhang, X.; Qian, M.; Faruque, O.; Brandt, M. SLM lattice structures: Properties, performance, applications and challenges. *Mater. Des.* **2019**, *183*, 108137. [CrossRef]
59. Alhammadi, A.; Khan, K.A.; Al-Ketan, O.; Ali, M.; Rowshan, R.; Al-Rub, R.K.A. Microstructural Characterization and Thermomechanical Behavior of Additively Manufactured AlSi10Mg Material and Architected Cellular Structures. In *TMS 2020 149th Annual Meeting & Exhibition Supplemental Proceedings*; Springer International Publishing: Berlin/Heidelberg, Germany, 2020; pp. 165–173.
60. Dong, G.; Tang, Y.; Li, D.; Zhao, Y.F. Design and optimization of solid lattice hybrid structures fabricated by additive manufacturing. *Addit. Manuf.* **2020**, *33*, 101116. [CrossRef]
61. EOS GmbH. 2022. Available online: https://www.eos.info/03_system-related-assets/material-related-contents/metal-materials-and-examples/metal-material-datasheet/aluminium/material_datasheet_eos_aluminium-alsi10mg_en_web.pdf (accessed on 29 January 2023).
62. Aboulkhair, N.T.; Maskery, I.; Tuck, C.; Ashcroft, I.; Everitt, N.M. The microstructure and mechanical properties of selectively laser melted AlSi10Mg: The effect of a conventional T6-like heat treatment. *Mater. Sci. Eng. A* **2016**, *667*, 139–146. [CrossRef]
63. Maamoun, A.H.; Elbestawi, M.; Dosbaeva, G.K.; Veldhuis, S.C. Thermal post-processing of AlSi10Mg parts produced by Selective Laser Melting using recycled powder. *Addit. Manuf.* **2018**, *21*, 234–247. [CrossRef]

64. Wu, G.; Li, G.; Pan, W.; Raja, I.; Wang, X.; Ding, S. A state-of-art review on chatter and geometric errors in thin-wall machining processes. *J. Manuf. Process.* **2021**, *68*, 454–480. [CrossRef]
65. Ferrar, B.; Mullen, L.; Jones, E.; Stamp, R.; Sutcliffe, C.J. Gas flow effects on selective laser melting (SLM) manufacturing performance. *J. Mater. Process. Technol.* **2012**, *212*, 355–364. [CrossRef]
66. Chen, X.X.; Tzeng, S.J.; Wang, W.C. Numerical and experimental observations of the flow field inside a selective laser melting (SLM) chamber through computational fluid dynamics (CFD) and particle image velocimetry (PIV). *Powder Technol.* **2020**, *362*, 450–461. [CrossRef]